PNAS RESEARCH ARTICLE | ENVIRONMENTAL SCIENCES

Cooperative mixing through hydrodynamic interactions in *Stylonychia lemnae*

Régis Turuban[a,b,1], Giovanni Noselli[b], Alfred Beran[c], and Antonio DeSimone[a,b,1]

Affiliations are included on p. 11.

Edited by Howard Stone, Princeton University, Princeton, NJ; received January 28, 2025; accepted July 27, 2025

Aquatic microorganisms typically inhabit a heterogeneous resource landscape, composed of localized and transient patches. To effectively exploit these resources, they have evolved a wide range of feeding strategies that combine chemotactic motility with active feeding flows. However, there is a notable lack of experimental studies that examine how these active flows shape resource fields to optimize feeding. In particular, the suspected cooperative hydrodynamics provided by groups of cells remains largely unexplored due to the difficulties in visualizing these dynamic three-dimensional flows. Here, we experimentally investigate how *Stylonychia lemnae* ciliates form feeding clusters of independent cells around food patches. Individual feeding flows interact hydrodynamically to create a chaotic collective flow at the population scale. Using a combination of experimental and numerical techniques, we measure and predict the entire collective flow, enabling us to assess its remarkable mixing and dispersion properties. We show that the active spreading of the food patch accelerates its detection by starving cells. As many fitness advantages provided by collective flows can be envisioned, we propose that this feeding cluster represents a form of intraspecific by-product cooperative behavior.

Stylonychia | intraspecific cooperation | feeding efficiency | chaotic mixing

Significance

To optimize foraging in a viscous environment, aquatic microorganisms use chemotactic motility or generate feeding flows. Some form colonies, possibly improving prey uptake through hydrodynamic interactions. In this study, we investigate how a group of *Stylonychia lemnae* ciliates interacts with food patches. As cells aggregate around a patch, they generate a chaotic collective flow that redistributes food within the population. We measure and predict the flow's properties, showing that it enlarges the food patch faster than individual swimming would, thereby accelerating food detection by starving cells. We interpret the behavior of the cluster as cooperative in terms of hydrodynamic interactions and emphasize the importance of accounting for the stochastic motions of individual cells that drive the chaotic flow.

Survival for aquatic microorganisms is about encountering: maximizing interactions with prey or nutrients for feeding and minimizing encounters with predators (1). Often, interactions are mediated by the chemical signals constantly released by microorganisms, whether they wish it or not. To best exploit patchy resource fields (2–5) in a viscous world, microorganisms have evolved the ability to navigate concentration gradients toward the source (chemotaxis) and/or actively generate flows powerful enough to shape concentration gradients directly. Examples of such actively generated flows include the currents around the organism's body as it swims (6–8), feeding flows produced by microorganisms either anchored to a solid substrate (9–13), tethered by gravity (14), or bonded together within a colony (15–18), as well as hydrodynamic waves triggered by rapid body contractions (19) or the long-range coherent flows produced by active suspension of pushers (20, 21). Faced with this diversity of cell organizations and their associated active flows, scientists have long wondered which fluid kinematics would lead to optimal feeding rates/nutrient uptake, and under which specific conditions.

Particularly well-suited to tackle this problem are the organisms exhibiting different morphotypes, ranging from unicellular to undifferentiated multicellular colonies. For example, refs. 15 and 22 have shown that *volvox* colonies—spherical colonies made up of thousands of Chlamydomonas cells bonded together—balance their expanding metabolic needs as their radius R grows by generating flows of increasing magnitude that steepen concentration gradients and thus ultimately enhance the diffusion flux, scaling just as the expanding surface $Q \sim R^2$. Other research by ref. 16 estimates that cooperative hydrodynamics within choanoflagellate colonies (which are attached together in the fluid bulk) increase the fresh fluid supply per cell compared to freely swimming single cells. However, another study by ref. 17 presents a contrasting view, predicting that choanoflagellate colonies are less advantageous in terms of feeding flux compared to single anchored cells, which in turn are less advantageous than freely swimming cells. Although the prediction that freely swimming provides the highest feeding rate is consistent with the results of ref. 23, it contradicts experimental findings indicating that cells tend to promote swimming over anchoring and feeding when deprived of food (24). Moreover, the claim that colonies are the least advantageous organization is challenged by the findings of ref. 25, which showed that in some choanoflagellate species, colony formation is triggered by sensing chemicals produced by their prey bacteria, even at very

Author contributions: R.T. designed research; R.T. performed research; R.T., G.N., and A.D. analyzed data; R.T. and G.N. designed experiments; A.B. grew cells and shared expertise on biology; A.D. supervised research, acquired funding; and R.T., G.N., A.B., and A.D. wrote the paper.

The authors declare no competing interest.

This article is a PNAS Direct Submission.

[1]To whom correspondence may be addressed. Email: rturuban@sissa.it or desimone@sissa.it.

This article contains supporting information online at https://www.pnas.org/lookup/suppl/doi:10.1073/pnas.2500588122/-/DCSupplemental.

Published September 8, 2025.

low concentrations. Clearly, the systematic feeding advantages conferred by diverse fluid kinematics—especially in the case of colonies—are still poorly understood.

To reconcile predictions with observations, a better understanding of the dynamic interaction between organisms and the nutrient/prey field is required. So far, the vast majority of studies have based their numerical estimations of feeding rates on strong simplifications: a cell generating a steady active flow, in a still ambient fluid, and immersed in a uniform resource field. The latter two conditions hold true only for $\mathrm{Pe}_{\mathrm{ambient}} < 1$, yet many organisms operate in the $\mathrm{Pe}_{\mathrm{ambient}} > 1$ regime (26) (where $\mathrm{Pe}_{\mathrm{ambient}} = v_{\mathrm{ambient}} L/D$ is the Péclet number relative to the ambient velocity field v_{ambient}, L the characteristic flow size, and D the diffusion coefficient). Regarding the first condition, unsteadiness is rarely discussed, although (27, 28) have demonstrated that the simple case of two nearby sessile cells alternating feeding currents can drastically enhance feeding by introducing Lagrangian chaos. In fact, experimental observations of microorganisms interacting with a resource field in the large Pe regime reveal much more dynamic behavior, as illustrated by the striking collective behavior exhibited by both the bacterium *Thiovulum majus* and the ciliate *Uronemella* (29–31). In this case, the authors suggest that the cell's oxygen consumption results from the highly dynamic interplay between three components: i) their locomotion behavior, which depends on gradients of both O_2 and population density; ii) the macroscopic active flow produced by the community, controlled by local population density; and iii) the O_2 concentration field advected by the macroscopic flow, and consumed by the cells. Thus, these studies underscore the need to revisit the feeding problem in a patchy food environment by taking into account this complex coupling. This requires experimental measurements of the evolving 3D active flow, which, to our knowledge, have not yet been performed.

Here, we propose to experimentally investigate the feeding behavior of *Stylonychia lemnae* (32) evolving in a patchy food environment. *S. lemnae* is a 200 μm long freshwater ciliate belonging to Spirotrichea, a class of ciliates widely distributed across diverse ecosystems, including freshwater, saltwater, soils, and activated sludge (33). *S. lemnae* can either swim or attach itself to interfaces and crawl. Being anchored to solid boundary allows the cell to exert a net force on the fluid using its adoral zone of membranelles (AZM; see Fig. 1 *A* and *B* and Movies S1 and S2), directing the fluid toward its buccal apparatus. Our research reveals that *S. lemnae* exhibits a collective feeding behavior that closely resembles that of *T. majus* and *Uronemella*, characterized by individual chemosensory locomotion to locate and remain near food patches, resulting in cell clustering around these patches. Next, multiple hydrodynamic interactions lead to flow at the population scale. However, unlike *volvox*, choanoflagellates colonies or the veils of *Uronemella*, where cells are bound together, the cells in *S. lemnae* feeding clusters remain strictly independent. This leads to an important question: Can such a loosely organized group of cells, lacking physical connections, exhibit cooperative behavior through hydrodynamic interactions? To this end, we experimentally characterize both locomotion behavior and the full 3D unsteady flow generated by a feeding cluster of *S. lemnae*. We numerically quantify the dispersion and mixing kinematics of the collective flow. By combining these two elements within the lamellar approach (34, 35), we are able to predict the rate at which any patchy resource field is distributed and homogenized within the feeding cluster.

1. Sensing Food Triggers a Change of Locomotion Behavior in *S.lemnae*

In laboratory conditions, when starving, *S. lemnae* typically wanders on the floor of a Petri dish looking for food, as illustrated in Fig. 1*D*. Thanks to its cirri, it crawls in wide leftward arcs over distances up to several millimeters, with an average speed of $\langle v_c \rangle \approx 790\,\mu\mathrm{m/s}$ ($\pm\sigma_{v_c} \approx 670\,\mu\mathrm{m/s}$), peaking at $v_c \sim 7{,}000\,\mu\mathrm{m/s}$ (i.e. $35L_c$/s, with $L_c \approx 200\,\mu\mathrm{m}$ the average cell length). The leftward arcs are interspersed with sudden stops ($v_c = 0$), which can last from a few tens of milliseconds to a few tens of seconds. Then, either the cell resumes its movement forward, or it performs abrupt moves called Side-Stepping Reactions (SSRs), typically observed in Spirotrich species such as *S. mytilus* or *Euplotes* (36–38). These movements involve two steps: bouncing backward, then rotating clockwise by a varying angle $\Delta\theta$. An example of a cell performing three successive SSR moves can be seen in Fig. 1*C*, resulting in that particular case in a complete revolution (Movie S3).

We noticed a drastic change in locomotion behavior whenever *S. lemnae* senses food. To quantify it, we conducted the following experiment. In the first step, the positions of starving cells are tracked for 5 min. In the second step, we inject food (either yeast or *Chlorogonium* algae) and gently stir it by hand until the food concentration is homogeneous inside the whole Petri dish. Another sequence of images is then taken for 5 min. Cell trajectories are reconstructed using particle tracking velocimetry (PTV) and Lagrangian velocities v_c extracted from displacements between successive images (*SI Appendix*, section 2A for details). A first qualitative difference of locomotion patterns can be inferred from the comparison between Fig. 1 *D* and *E* (Movie S4). Clearly, cells deprived of food travel much farther, whereas cells in the presence of food shorten their crawling segments and make longer stops. With reduced travel, SSR movements mostly result in rotation around a point, with minimal drift. At the macroscopic scale, this behavioral change is quantified by the mean squared displacement (MSD), defined as the variance of cell displacements $\sigma_{\boldsymbol{x}}^2 = \langle |\boldsymbol{x}(t) - \boldsymbol{x}(0)|^2 \rangle$, with $\langle \ldots \rangle$ the ensemble average over all trajectories i, after checking that cell spreading is isotropic, i.e. $\langle \boldsymbol{v_c} \rangle = 0$. The MSDs for both cases are compared in Fig. 1*G*. The MSD for the no-food case well captures the early-time ballistic regime $\sigma_{\boldsymbol{x}}^2 \sim t^2$. After a coherence time, the MSDs shift to a diffusive regime $\sigma_{\boldsymbol{x}}^2 \sim t$, but this regime is soon limited by the finite imaging area (cells exiting the field of view). To overcome this limitation and get the asymptotic scaling, we compute the MSD from the velocity autocorrelation function (VAF) (*SI Appendix*, section 2B), which are related through the expression $\sigma_{\boldsymbol{x}}^2 = 2\int_0^t d\tau (t-\tau) C(\tau)$, with $C(\tau) = \langle \boldsymbol{v_c}(\tau) \cdot \boldsymbol{v_c}(0) \rangle$, whose graphs are displayed in Fig. 1*F*, as a function of the time lag $\tau = t' - t''$. The new MSD graphs are superimposed onto the previous MSDs in the same Fig. 1*G*, and reveal that both MSDs reach a Fickian regime $4Dt$, though with a dispersion coefficient D that varies with ambient conditions. These dispersion coefficients are computed via the Green–Kubo relation $D = \frac{1}{2}\int_0^\infty d\tau \langle \boldsymbol{v_c}(\tau) \cdot \boldsymbol{v_c}(0) \rangle$. We get $D_{\mathrm{NF}} = 4.3 \times 10^{-7}\ \mathrm{m^2/s}$ (no-food) and $D_{\mathrm{WF}} = 4.5 \times 10^{-8}\ \mathrm{m^2/s}$ (with-food), indicating that cells span space $D_{\mathrm{NF}}/D_{\mathrm{WF}} \approx 10$ times slower when food is present. This drop is due in part to the slightly faster decay of $C(\tau)/C(0)$ as shown in Fig. 1*F*, but mostly from an overall reduction in locomotion speed v_c through the ratio $C(0)_{\mathrm{NF}}/C(0)_{\mathrm{WF}} = \langle \boldsymbol{v_c}^2 \rangle_{\mathrm{NF}} / \langle \boldsymbol{v_c}^2 \rangle_{\mathrm{WF}} \approx 4.7$. This is confirmed by the velocity distribution $P(v_c)$ shown in

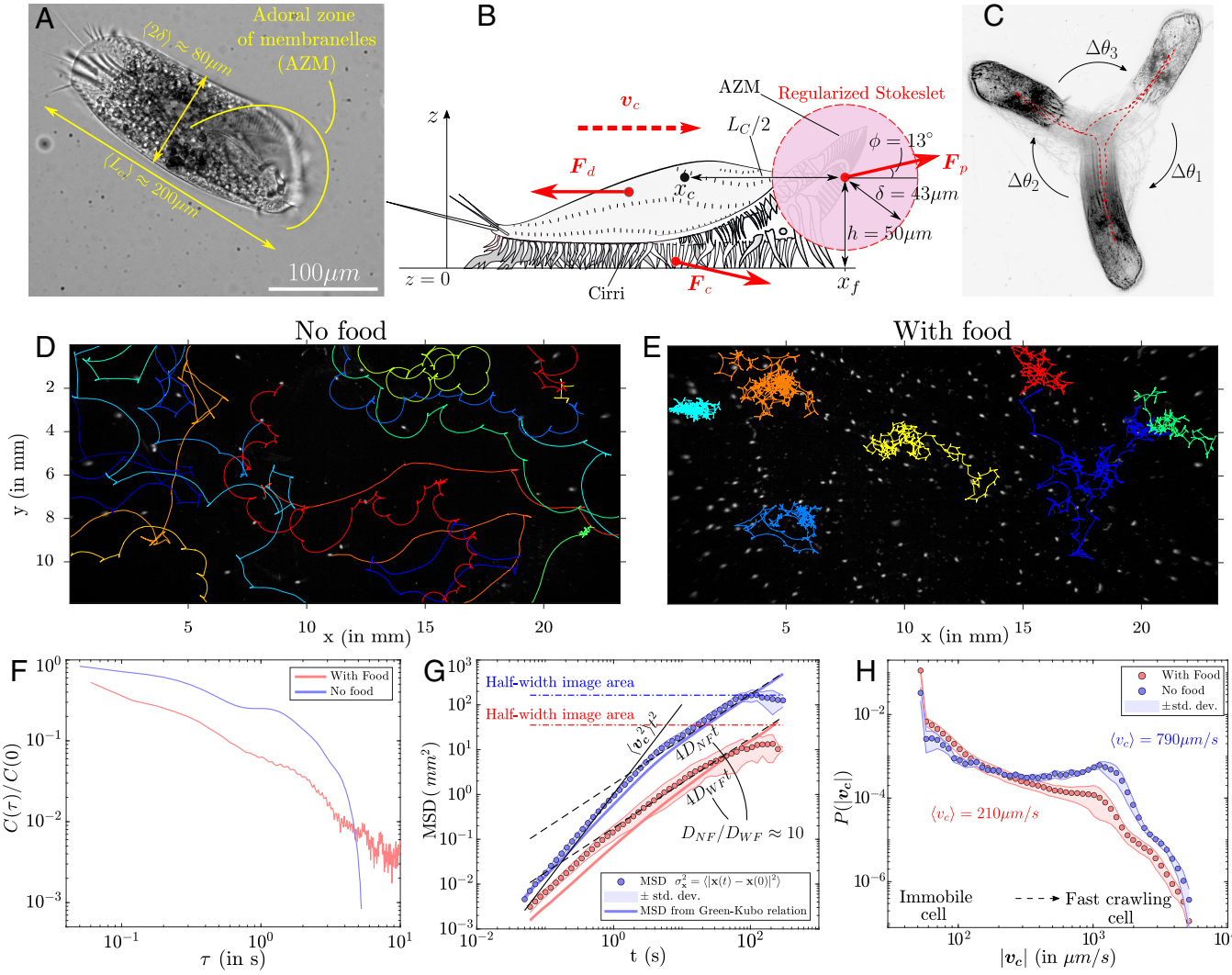

Fig. 1. *S. lemnae*'s locomotion behavior. (*A*) Microscopy image of a *S. lemnae* cell viewed from below. (*B*) Schematic lateral view (adapted from the *Stylonychia* Wikipedia webpage), and the balance of forces acting on the cell body during crawling locomotion at speed v_c. (*C*) A *S. lemnae* cell performing a series of three Side-Stepping Reactions (SSRs). The cell's trajectory is displayed as a red dashed line. (*D*) Trajectories $\boldsymbol{x}_i(t)$ followed by starving *S. lemnae* as they crawl on the bottom of their Petri dish culture. (*E*) Trajectories followed by the same cells ∼1 to 2 min after the injection and manual mixing of food. These trajectories are selected so that they do not overlap. (*F*) Normalized autocorrelation function of the crawling velocities $\boldsymbol{v_c}$ (VAFs) for the two distinct ambient conditions: no food (in blue) and with food (in red). (*G*) Mean square displacement (MSD) calculated either from the variance of cell displacements (dots), or from the Green–Kubo relation (continuous lines), computed from the VAFs in panel (*F*). Same color code as before. Error bars (shaded area) indicate the SD across seven different datasets. The continuous black line represents ballistic transport at early times, scaling as $\sigma_{\boldsymbol{x}}^2 \sim \langle \boldsymbol{v_c}^2 \rangle t^2$, for the no-food case. The black dashed lines represent the asymptotic Fickian regime $\sigma_{\boldsymbol{x}}^2 \sim 4Dt$ reached in both cases, with different dispersion coefficient D_{NF} (no-food) and D_{WF} (with-food). The colored dashed lines indicate the image boundary beyond which cells are out of view. (*H*) Probability density function of cell speed $P(|\boldsymbol{v_c}|)$ under the two ambient conditions. The minimum measurable velocity with our setup is $v_c^{\min} = 50\,\mu$m/s, below which the cell is considered immobile.

Fig. 1*H*, which reveals that food injection triggers a massive drop in high-speed events, with a fivefold drop in mean speed $\langle v_c \rangle$. Thus, cells switch between two locomotion modes depending on food availability, primarily by modulating v_c–a well-known chemotactic strategy to remain in favorable areas (39).

2. Formation of a Cluster of Feeding Cells Around a Food Injection Site and Collective Fluid Mixing

To mimic the patchy food environment in which many organisms live (2, 3), we conduct a similar experiment, with the difference that the food is now injected within a confined region (*SI Appendix*, section 3). About $M_{\mathrm{yeast}} = 0.25 \pm 0.10$ mg of yeast (i.e. almost three orders of magnitude larger than the amount a single cell can consume, assuming it can ingest up to 25% of its own volume) is injected at position $\mathbf{x}_{\mathrm{inj}}$ among starving crawling cells (see Fig. 2 *A*, (*i*) and *SI Appendix*, Fig. S2, extracted from Movies S5 and S6, respectively). The food blob is originally $s_0 \approx 0.5$ mm $= 2.5L_c$ in diameter. Before injection, cells exhibit persistent long traveling paths that frequently reach values up to $20L_c$ (with peaks of $50L_c$), when integrated over a period of 5 s. Immediately after injection (Fig. 2 *A*, (*i*), $t = 5$ s), only cells that come into contact with the injected food blob drastically reduce their traveled path but, over time, even distant cells restrict their amplitude of motion (Fig. 2 *A*, (*ii*), $t = 280$ s). The transition toward shortened movement over time is shown in Fig. 2*B*. After $t = 400$ s, most cells no longer travel, even those far from the injection point (up to 1 cm, i.e. $20s_0$): A feeding cell cluster has formed. The phenomenon is all the more intriguing given that yeast diffuses very slowly, with $D_{\mathrm{yeast}} \approx 10^{-11}$ m^2/s as given by the Stokes–Einstein equation. Importantly, cluster

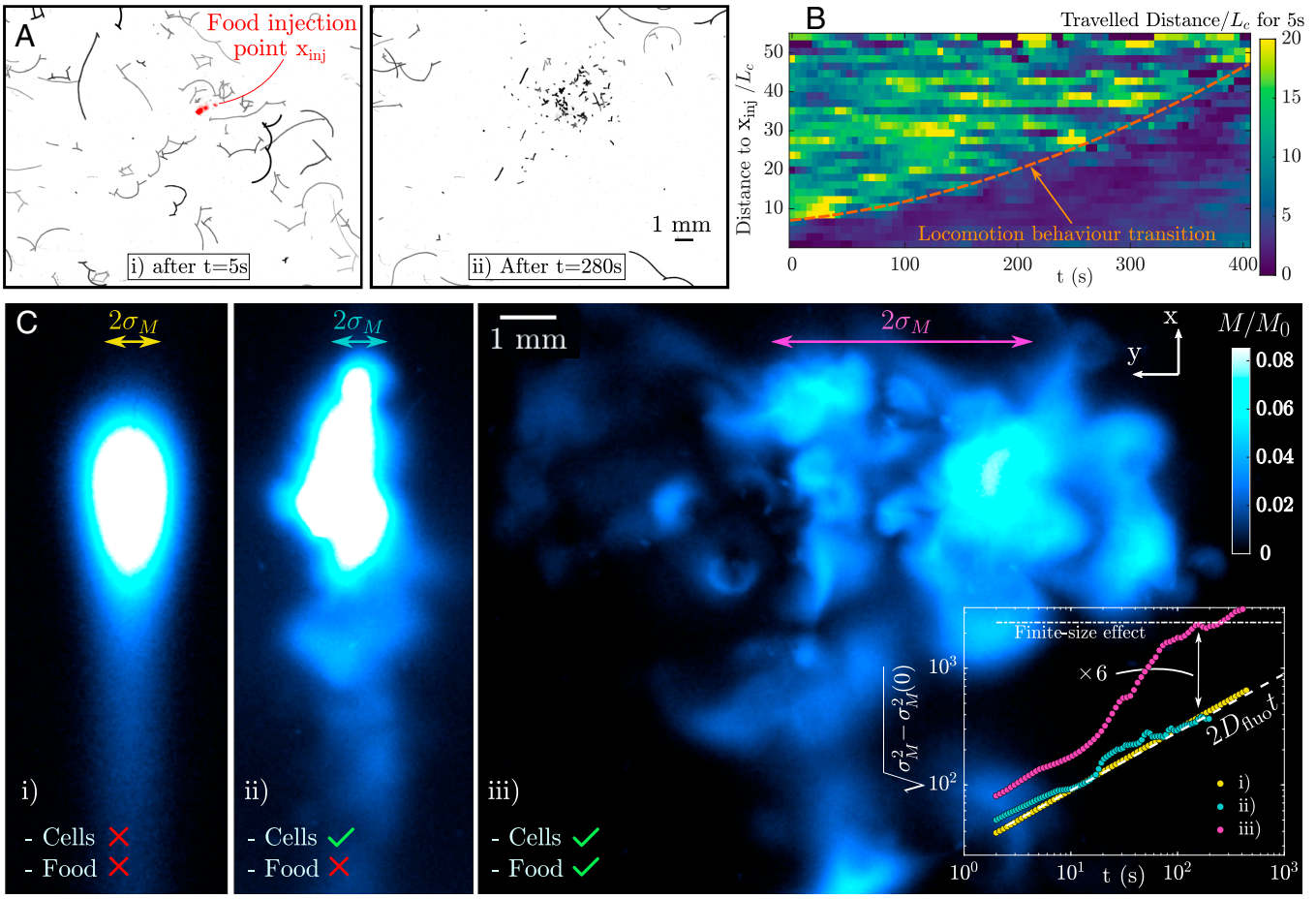

Fig. 2. Collective flow by a feeding cell cluster. (*A*) Trajectories of a few *S. lemnae* integrated over 5 s, from i) $t = 5$ s and ii) $t = 280$ s after the local injection of yeast, at position x_{inj}. (*B*) Temporal evolution of the distance traveled by different *S. lemnae* over 5 s, depending on their initial distance from the food injection point x_{inj}. The statistical analysis is based on ≈640 trajectories from one experiment. The orange continuous line shows the transition between the two locomotion behavior triggered further and further away from the food injection point as time progresses. Initially, about 50 cells are visible on the images, progressively increasing to reach up to 100 cells, 400 s after the injection. (*C*) Imaging of a fluorescein blob injected in the observation chamber either i) in the absence of *S. lemnae* cells, or ii) injected among cells, or iii) mixed with yeast prior to injection among cells. These snapshots were taken at $t = 174$ s after the injection of the dye blob. Fluorescence intensity levels $I(x, y)$ are converted to mass levels $M(x, y)$ normalized by the initial mass M_0. *Inset*: Temporal evolution of the spatial variance of fluorescein mass in the *y*-direction, $\sqrt{\sigma_M^2 - \sigma_M^2(0)}$, for the 3 cases. The yellow, cyan, and purple arrows superimposed on the images depict the width $2\sigma_M$ of the Gaussian function that would fit the *y*-profile of the three mass fields.

formation is consistently reproducible, regardless of the cells' food vacuole fullness. Indeed, although at the high initial food concentration the cells may become fully fed in just a few seconds and stop ingesting food (Movie S7), this does not affect their locomotion behavior, which depends primarily on the detected food concentration (*SI Appendix*, section 4).

To understand how food detection by cells occurs at an increasing distance from the injection point, and to reveal any potential flow, we perform a passive solute tracer experiment by injecting a mixture of yeast with fluorescein-dyed water among a group of *S. lemnae*. To do so, a few tens of cells are transferred to an observation chamber consisting of two parallel glass plates separated by a 3 mm gap, large enough to avoid confinement effects (40). The dyed mixture is injected using a syringe, and imaging begins promptly after its withdrawal. The evolving fluorescein field is imaged using LED-Induced Fluorescence (LEDLIF), where the fluorescence intensity field $I(x, y)$ in the raw image is converted to mass $M(x, y)$ of fluorescein accumulated in the z-column above each pixel (x, y), via the linear relation $M(x, y) \propto I(x, y)$ (see *SI Appendix*, section 5 for the full procedure).

We compare tracer transport in the presence of food to two control experiments: i) pure diffusion, with fluorescein injected in the observation chamber without cells, and ii) fluorescein injected among cells but without yeast. Fig 2*C* shows images of the dye blobs from each of the three experiments, taken 3 min after injection (Movie S8). In the cell-only case ii), the dye blob undergoes some local and intermittent stirring, but its final shape is quite similar to that of the purely diffusive case i). By contrast, Fig 2 *C*, (*iii*) reveals how *S. lemnae* cells, in the presence of food, actively generate a large-scale chaotic flow that, in turn, dramatically reshapes and spreads fluorescein throughout the observation chamber. The steep mass gradients consistently observed throughout the experiment indicate an active Péclet number higher than unity $\mathrm{Pe}_{\mathrm{active}} = vd/D_{\mathrm{fluo}} > 1$, with $D_{\mathrm{fluo}} \approx 4.10^{-10}\,\mathrm{m}^2/\mathrm{s}$ the theoretical molecular diffusion coefficient of fluorescein (i.e. only five times lower than the oxygen diffusion coefficient $D_{O_2} \approx 2.10^{-9}\,\mathrm{m}^2/\mathrm{s}$). A more quantitative comparison between the tracer experiments can be made by measuring the spatial variance of the mass field in the y direction: $\sigma_M^2 = \Sigma_i (y_i - \mu)^2 M(x_i, y_i)/\Sigma_i M(x_i, y_i)$, with $\mu = \Sigma_i y_i M(x_i, y_i)/\Sigma_i M(x_i, y_i)$ the mass-weighted mean position

and (x_i, y_i) the position of the pixel i. The graphs are shown in the *Inset* of Fig 2*C*. As expected in the pure diffusive case, the mass variance follows the linear law $\sigma_M^2 = 2D_{\text{fluo}}t$. Case ii) displays a very similar scaling. Whereas in case iii) where both cells and food are present, after an initial transition time, σ_M^2 exhibits superdiffusive growth $\sigma_M^2 \sim t^\alpha$ with $\alpha > 1$ for over a decade in time, until the dye blob reaches the chamber boundaries at $t \approx 200$ s. The ratio of characteristic spreading lengths σ_M between tests i) and iii) reaches a maximum of ~6. These results demonstrate how just a few dozen *S. lemnae* can generate chaotic flows that powerfully spread and mix any dissolved or suspended substances, even within the constraints of Stokes flow. One can extrapolate this observation to natural situations where potentially much larger clusters composed of many more individuals form.

3. Hydrodynamic Disturbances Produced by a Single *S.lemnae* Either Fast Crawling or Anchored

3.1. Experimental Measurements. How does a collective flow emerge and how does it relate to the switch in locomotion behavior pointed out in an earlier section? Answering this question requires one to experimentally examine the hydrodynamic disturbances produced by a single cell. We measure and compare the flow in the cell vicinity during the two main locomotion behaviors described previously, i.e. either fast crawling ($v_c \gg 0$) or anchored ($v_c \approx 0$) on a no-slip boundary. In the observation chamber, we inject water containing microbeads that are used as passive tracers to visualize the flow. Since we are ultimately interested in fluid transport and mixing, we use PTV which, unlike Eulerian approaches, provides the essential information about net fluid displacement (*SI Appendix*, section 6A).

The recorded trajectories of microtracers affected by the motion of three fast crawling cells (Movie S9), with crawling speeds around $v_c \approx$ 1,000 to 1,500 μm/s, are gathered and shown in Fig. 3*A* in a single cell frame (see *SI Appendix*, section 6B for the transformation from the lab frame to the cell frame). The tracers move over a persistence time of about $T_p = 0.5$ s. We define the persistence time T_p as the time during which tracers move due to the cell's hydrodynamic perturbation $\boldsymbol{v}(\boldsymbol{x})$ (i.e. above the Brownian motion due to thermal agitation) which for large v_c varies as $T_p \sim 1/v_c$. Microtracers ahead of the cell are first pumped toward the buccal apparatus before being dragged back in the cell's wake as it crawls past the tracers. The general pattern of tracer trajectories reveals a very short-range flow, with those on both lateral sides of the cell resembling the closed loops described by ref. 42, who modeled fluid particle displacement by squirmers. For such trajectories, the net displacement of tracers mostly cancels. A significant net displacement $\Delta x \sim L_c$ can only be found for the tracers located on the cell's path, i.e., for the ones coming into close contact with the stagnation points near the cell body. Indeed, a moving cell can bring in its wake some fluid over even longer distances ("Darwin drift"), though this is typically limited to a very small volume (Movie S10). On the other hand, we measure the feeding flow produced by an anchored cell (*SI Appendix*, section 6C and Movie S11), an example of which is displayed in Fig. 3*B*. In this example, lasting $T_p = 7.6$ s, the flow is unidirectional, and the net tracer displacement reaches distances up to 5 to $6L_c$. We can qualitatively see from the direct comparison between the two cases that the long-range feeding flow is considerably more efficient at transporting fluid over long distances, and this is all the more true as the cell remains motionless and feeds. While feeding, *S. lemnae* remains motionless on average for a few seconds and may reach pumping times of ~100 s.

3.2. Modeling the Individual Feeding Flow by a Regularized Stokeslet above a No-Slip Plane. We model the single feeding flow by a regularized (volume) Stokeslet above a wall, from the theory developed by refs. 41 and 43 (*SI Appendix*, section 6D). The model needs five parameters: the location of the force $\boldsymbol{x}_f$ in the xy plane, its height h above the wall, the radius of the force δ, the 3D orientation of the force $\boldsymbol{F}_p/|\boldsymbol{F}_p| = (\cos\theta\cos\phi, \sin\theta\cos\phi, \sin\phi)$ (where θ and ϕ are, respectively, the angle with respect to the x axis in the xy plane and the angle with respect to the wall $z = 0$) and its magnitude $F_p = |\boldsymbol{F}_p|$. The parameters $\boldsymbol{x}_f$, h, δ and ϕ are fixed and extracted from the anatomical features of *S. lemnae* (see the scheme of Fig. 1*B*). The force is located at $\boldsymbol{x}_f = \boldsymbol{x}_c - (L_c/2)\boldsymbol{F}_p^{xy}/|\boldsymbol{F}_p|$, where $\boldsymbol{x}_c$ is the cell center, L_c its average length, and $\boldsymbol{F}_p^{xy}/|\boldsymbol{F}_p| = (\cos\theta, \sin\theta)$ the force orientation in the xy plane. The parameter h is the height of the cell's anterior above the plane and the force radius δ is taken as the cell's half-width. The angle ϕ with respect to the $z = 0$ wall is measured from the systematic inclination of the cell's anterior toward the top. In summary, we measure on average $L_c \approx 200$ μm, $h \approx 50$ μm, $\delta \approx 43$ μm, and $\phi \approx 13°$. These values are held constant across all cells, ignoring the slight variation in their size. Only the cell position $\boldsymbol{x}_c$ and orientation θ vary and will be extracted systematically from images. In Fig. 3*C*, analytical streamlines are compared to a set of experimental streamlines consisting in nine individual feeding flows superimposed all together, produced by nine different cells of slightly varying size, with $Lc = 200 \pm 20$ μm (*SI Appendix*, section 6C–E). Visual comparison between analytical and experimental streamlines shows a nearly perfect geometrical match, thus validating the model. Note that the flow is inherently 3D, as the wall imparts parallel shear and bending of the streamlines in the transverse z-direction (*SI Appendix*, Fig. S5*A*). Last, the force magnitude $|\boldsymbol{F}_p|$ is obtained by least-squares fitting of analytical and experimental velocity magnitudes, yielding $|\boldsymbol{F}_p| = 1{,}200 \pm 240$pN (*SI Appendix*, section 6E). This value is consistent with reported force magnitudes for other attached filter feeders when plotted as a function of cell dimension; see *SI Appendix*, Fig. S6. The main source of error in estimating $|\boldsymbol{F}_p|$ stems from the slight variability in cell size L_c, and we expect it to be the main source of error for computing the total collective flow as well. These velocity field measurements allow us to estimate both Reynolds and Péclet numbers. The Reynolds number is $Re = vL/\nu$, with L the characteristic feeding flow size, v the fluid velocity and $\nu \approx 10^{-6}$ m^2/s the kinematic viscosity of water. Taking $L = 500 \times 10^{-6}$ m and $v = 100 \times 10^{-6}$ m/s, we get $Re = 0.05 \ll 1$, ensuring Stokes conditions. The Péclet number for the fluorescein experiment shown in Fig. 2 is estimated as $\text{Pe}_{\text{active}} = vL/D_{\text{fluo}} \approx 125$, and for oxygen, $\text{Pe}_{\text{active}} \approx 25$. Given the reported diffusivity of dissolved organic matter ranging from $D = 10^{-12}$ to 10^{-9} m^2/s (44), the corresponding Pe_{active} spans 50 to 50,000, giving a first hint of the dominance of feeding flows over diffusion for many nutrients.

3.3. The Locomotion Speed Determines the Type of Hydrodynamic Disturbance. We explain the origin of the two hydrodynamic disturbances using the balance of forces applied to the cell while crawling at a given speed v_c (see scheme of Fig. 1*B*). The drag force $\boldsymbol{F}_d$ opposes two propulsive forces, i.e. the pumping force $\boldsymbol{F}_p$ generated by its AZM and the contact

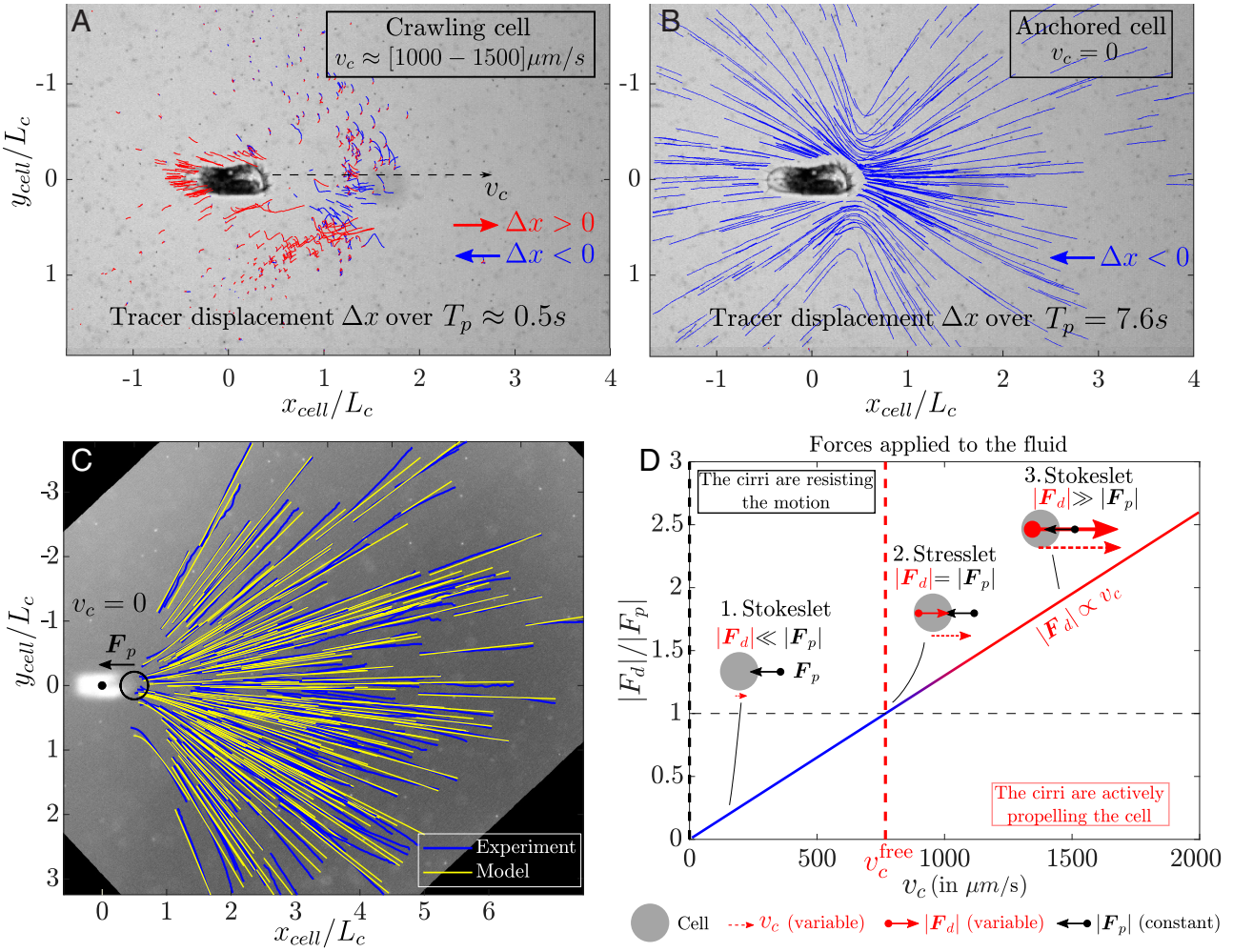

Fig. 3. Comparison of the hydrodynamic disturbances caused by an isolated *S. lemnae* either (*A*) crawling ($v_c \gg 0$) or (*B*) immobile ($v_c \approx 0$), projected in the *xy* plane, in the cell frame. In the crawling case (*A*), fluid particles are displaced over a persistence time about $T_p \approx 0.5$ s. In the immobile case (*B*), the cell remains anchored for $T_p = 7.6$ s. In both cases, fluid particles trajectories are colored blue if they move left ($\Delta x < 0$) or red if they move right ($\Delta x > 0$). (*C*) Comparison between the experimentally measured streamlines (in blue) ahead of a feeding cell and the theoretical streamlines predicted by the model of ref. 41 (in yellow), in the *xy* plane. The black dot marks the center of the ellipsoid matching the cell's body $\boldsymbol{x}_c = (0, 0)$, and the black circle indicates the position $\boldsymbol{x}_f$ and radius δ of the volume force. (*D*) Relative importance of the magnitude of the two opposite forces applied to the fluid by the action of the cell (depicted as a gray disk), i.e. drag force F_d vs. pumping force F_p. F_p is assumed to be constant, while F_d scales as $F_d \propto v_c$. Depending on the ratio F_d/F_p, three distinct scenarios for the far-flows are identified: 1) Immobile or slow-moving Stokeslet above a wall, with $\boldsymbol{F}_p$ opposite to the cell's motion. 2) Stresslet above a wall, at the terminal velocity $v_c^{free} \approx 770\,\mu$m/s. 3) Fast-moving Stokeslet $\boldsymbol{F}_d$ aligned with the cell's motion.

force $\boldsymbol{F}_c$ between the cirri and the solid substrate. Hence, for a cell crawling in a straight line at constant speed, we have the balance of forces $\boldsymbol{F}_d = -(\boldsymbol{F}_c + \boldsymbol{F}_p)$. Since drag is proportional to speed $\boldsymbol{F}_d = -C_d \boldsymbol{v_c}$ (with C_d the drag coefficient whose value is estimated in *SI Appendix*, section 7), the cell speed $\boldsymbol{v_c}$ is given by

$$\boldsymbol{v_c} = \frac{1}{C_d}(\boldsymbol{F}_c + \boldsymbol{F}_p). \qquad [1]$$

In what proportion do these two forces contribute to v_c? Based on observations that the AZM appears to be consistently active during both crawling and pumping, we assume that the pumping force magnitude $|\boldsymbol{F}_p| = 1{,}200$ pN remains constant. Only during brief SSR events or rare mitosis does the AZM seem to stop. In the event that $\boldsymbol{F}_p$ was the only propulsive force and $\boldsymbol{F}_c = 0$, $\boldsymbol{F}_d$ would balance $\boldsymbol{F}_p$ at a terminal speed $v_c \approx 770\,\mu$m/s (see again *SI Appendix*, section 7). Yet, *S. lemnae* can achieve much greater locomotion speed, up to $v_c \sim 7{,}000\,\mu$m/s, as can be seen in Fig. 1*H*, which suggests that the force $\boldsymbol{F}_c$ plays a driving role in the crawling mode.

How do these forces impact the surrounding fluid? While three forces act on the cell, only two forces are exerted by the cell on the fluid, namely the opposite forces $-\boldsymbol{F}_p$ and $-\boldsymbol{F}_d$. In fact, the contact force $\boldsymbol{F}_c$ between the cirri and the wall is assumed to be fully transmitted to the substrate and to have no effect on the fluid. However, $F_c = |\boldsymbol{F}_c|$ as an external force ultimately determines the amount of drag force $F_d = |\boldsymbol{F}_d|$, since $F_d \propto v_c$, and $v_c \propto F_c$ according to Eq. **1**. As a consequence, we end up with three regimes of far-field flows, depending on the relative importance of F_d over the constant F_p, as summarized in Fig. 3*D*. When the cell is immobile ($v_c = 0$; see Fig. 3*B*) or crawling slowly, such that $F_d/F_p \ll 1$, it produces an unaltered pumping flow, approximated as a Stokeslet above a wall, decaying as $v \sim 1/r^2$, and opposite to the cell's motion. When $F_d/F_p = 1$ (i.e. for $v_c^{free} \approx 770\,\mu$m/s), and neglecting the slight inclination of $\boldsymbol{F}_p$ with respect to $\boldsymbol{F}_d$ as shown in Fig. 1*B*, the far field corresponds to a stresslet (dipole force) above a wall that decays as $v \sim 1/r^3$ (45), producing fluid trajectories close to those shown in Fig. 3*A*. In this specific case, no net force is exerted

on the fluid. Finally, when the cell reaches high speed for which $F_d/F_p \gg 1$, the far field is again a Stokeslet above a wall, but aligned with the cell's motion.

3.4. Either the Cell Moves or it Moves the Fluid. The origin of collective flow lies in the ability of a single hydrodynamic disturbance to displace fluid over distances Δx comparable to separation distances between feeding cells d_c. In fact, the far-field flows pointed out in the previous section induce very different net fluid displacements. The net tracer displacement $\Delta x = |\boldsymbol{x} - \boldsymbol{x_0}|$ is computed by integrating the advection equation $\dot{\boldsymbol{x}} = \boldsymbol{v}(\boldsymbol{x}(t), t)$ from an initial position $\boldsymbol{x_0}$:

$$\Delta x = \left| \int_0^{T_p} \boldsymbol{v}(\boldsymbol{x}(t), t) dt \right| . \qquad [2]$$

Two main factors influence Δx: the nature of the velocity vector field $\boldsymbol{v}(\boldsymbol{x})$ (e.g. whether it is unidirectional and how it decays spatially $v \sim 1/r^n$), and the persistence time T_p. Stokeslets transport fluid more effectively than stresslets, as already clear from the comparison between Fig. 3 *A* and *B*. Then, among the two main scenarios involving Stokeslets (1 and 3 in Fig. 3*D*), the persistence time T_p makes the difference: At constant force magnitude, the total fluid volume moved is the same, but faster-moving cells interact with more particles, displacing each one less on average (*SI Appendix*, section 8). In brief, the feeding flow range is maximum for $v_c = 0$, and any increase in v_c reduces it, both because $F_d \propto v_c$ and $T_p \propto 1/v_c$ (*SI Appendix*, section 8). Thus, the difference in hydrodynamics observed between Fig. 2 *C*, (*ii*), and (*iii*) is explained by the global reduction of v_c triggered by food injection, as observed in earlier section. In short, either the cell moves or it moves the fluid. Then, considering that the feeding cells remain immobile over $\tau_c \approx 2$ s on average (as shown later in Section 5), in such a case, the feeding flow extends up to $\Delta x \sim 2.5 L_c$ in the xy plane. This is comparable to the average separation distance between feeding cells measured in the experiment illustrated in Fig. 2 *A*, (*ii*), which gave $\langle d_c \rangle \sim 4.5 L_c$, so that $\Delta x \sim \langle d_c \rangle / 2$, implying that pumping flows interact hydrodynamically (*SI Appendix*, section 9 for the method to measure d_c). In the following collective flow model, we disregard the hydrodynamic contributions of the last two scenarios by setting a maximum locomotion speed threshold $v_c^{\max}$ over which cells are considered to exert no force on the fluid. We select $v_c^{\max} = 500$ µm/s, after noticing that the proportion of feeding cells varies little with the choice of $v_c^{\max}$ between 300 µm/s and 700 µm/s (*SI Appendix*, section 17).

4. Characterization of the Collective Feeding Flow

4.1. Analytical Skin Friction Field on the Solid Boundary. To quantify the strong mixing and dispersion properties of the collective flow observed in Fig. 2, one would ideally need access to the full, time-evolving 3D velocity field. We here overcome this experimental challenge by demonstrating that the flow can be entirely inferred from its salient topological features (46), which stem from stagnation (critical) points of the skin friction field on the wall. To illustrate this concept, we consider a simple case where two cells pump in opposite directions, and predict how the resulting flow organizes the spatial distribution of a cloud of tracers (2 µm microbeads mixed with *Chlorogonium*-free medium) injected nearby (Fig. 4*A* and Movie S12). Given the linearity of the Stokes equation, the total velocity field $\boldsymbol{v}$ at time

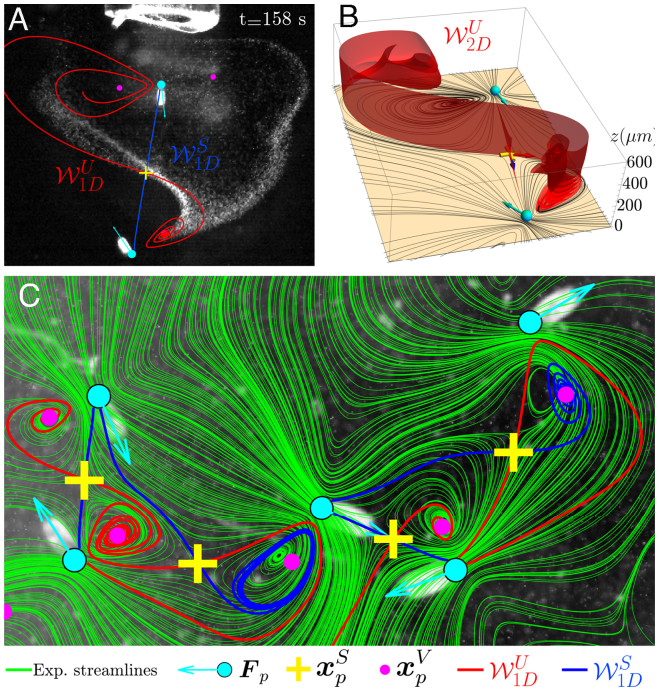

Fig. 4. (*A*) Image of two *S. lemnae* oriented in opposite directions while feeding on a mixture of *Chlorogonium*-free medium and tracer beads (appearing as a cloud of white dots, injected 158 s earlier from the syringe tip visible at the top). Superimposed on the image are the numerical 1D manifolds $\mathcal{W}_{1D}$ emerging from the hyperbolic point $\boldsymbol{x}_p^S$ of the analytical skin friction field, computed by summing the two volume forces (with positions and orientations extracted from the cell images, depicted as cyan dots and arrows respectively). (*B*) Associated 2D manifold $\mathcal{W}_{2D}$ repelled from $\mathcal{W}_{1D}$ of the skin friction field (whose streamlines are displayed as continuous black lines lying on the $z = 0$ plane) generated by the configuration of cells shown in (*A*). (*C*) Instantaneous streamlines (in green) of the experimentally measured velocity field in the $z = 150$ µm plane, produced by a group of feeding cells. Superimposed are the 1D manifolds $\mathcal{W}_{1D}$ from the associated analytical skin friction field. For clarity, $\mathcal{W}_{1D}$ are truncated at intersections with volume forces.

of image t_j and position $\boldsymbol{x} = (x, y, z)$ is simply the sum of all N single pumping flow $\boldsymbol{v}_i(\boldsymbol{x}, t_j)$:

$$\boldsymbol{v}(\boldsymbol{x}, t_j) = \sum_{i=1}^{N} \boldsymbol{v}_i(\boldsymbol{x}, t_j) . \qquad [3]$$

where each $\boldsymbol{v}_i$ depends on the position and orientation of the cell i (provided $v_c < v_c^{\max}$). Similarly, the skin friction field on the wall $z = 0$, defined as $\boldsymbol{\tau}_i(x, y) = \partial \boldsymbol{v}_i / \partial z|_{z=0}$, is also additive, so that the total skin friction is $\boldsymbol{\tau}(t_j) = \sum_{i=1}^{N} \boldsymbol{\tau}_i(t_j)$. In the example of Fig. 4*A*, since the two cells are pumping in opposite directions, a stagnation point must lie on the wall between them, meaning that the skin friction field cancels at a critical point $\boldsymbol{x}_p$, defined as $\boldsymbol{\tau}(\boldsymbol{x}_p) = 0$. This critical point is found to be a saddle point $\boldsymbol{x}_p^S$ (*SI Appendix*, section 10B). Surana et al. (47) demonstrate that saddle points of the skin friction field are the starting/ending points of 2D manifolds $\mathcal{W}_{2D}$, which act as separation/reattachment material surfaces that propagate in the fluid interior. The 2D stable/unstable manifolds are computed numerically by advecting backward/forward in time some tracer particles initially placed just above the detected separation/reattachment critical skin friction lines (see example of $\mathcal{W}_{2D}$ of Fig. 4*B*, coming from $\mathcal{W}_{1D}^S$ of Fig. 4*A*). These 2D surfaces are crucial in our system for two reasons: First, they are surfaces with locally minimal flux, thus

forming a flow skeleton (48) that governs fluid transport; second, because they also induce exponential stretching or compression of nearby fluid elements, they coincide with part of the Lagrangian Coherent Structures (LCSs) that control fluid deformation, and ultimately mixing (46). Getting back to our example seen in Fig. 4 *A* and *B*, the influence of the 2D unstable manifold $\mathcal{W}^U_{2D}$ on the spatial distribution of the cloud of tracers is evident: $\mathcal{W}^U_{2D}$ attracts the cloud, which ultimately fits its shape, perfectly in the *Bottom Right* of the image, whereas the syringe tip and an off-frame cell distort the tracers distribution in the *Top Left* corner. Nevertheless, the global match illustrates that 3D tracer dynamics can be predicted from analytical critical skin friction lines alone. Next we check that the experimental flow patterns can be systematically predicted for the many diverse configurations of cell number, relative positions, and orientations encountered through the imaging. It should be noted that, because our flow is said "open" (the flow intensity vanishes in the z direction), the criteria for defining reattachment/separation surfaces (47) are not always strictly fulfilled. Anyway, we show in *SI Appendix*, section 10C that this has little importance as long as we do not look too far from the bottom wall $z = 0$.

4.2. Velocity Field Measurement and Comparison with the Analytical Skin Friction Field. For each image, the collective velocity field within a feeding cell group is measured using Particle Image Velocimetry (PIV) in a focal plane set at $z_{fp} = 3h$ above the bottom plate. We inject a mixture of water seeded with microbeads and containing just enough *Chlorogonium* cells to spark the feeding behavior in *S. lemnae*. We get the instantaneous flow by computing the streamlines—curves tangent to the velocity vector field—at each time step (*SI Appendix*, section 10A), with examples shown in Fig. 4*C* and *SI Appendix*, Fig. S9 and Movies S13 and S14. Rich flow patterns can be observed, with a mingling of saddle points and vortices forming, bifurcating and breaking over time, as the cells crawl, stop, and reorient. On these experimental streamlines, we overlay critical points and skin friction lines calculated from the same configuration of cell positions and orientations. Although we compare two sets of streamlines that are separated vertically by $z = 3h = 150\,\mu$m, we assume this gap is small enough so that the sketch drawn by the critical skin friction lines $\mathcal{W}_{1D}$ on the wall is representative of the flow patterns in the measurement plane. Within the resolution limits, and provided no off-frame cell alters the flow within the frame, the agreement between experimental and analytical patterns is remarkable, regardless of cell number, separation distance, or orientation. The minor discrepancies sometimes observed likely stem from the finite-size distribution of cell sizes (and so of the pumping force $|\boldsymbol{F}_p|$), which is not included in our model. We emphasize that our collective flow model is all the more reliable because the feeding force never fluctuated throughout the experiments, even when the cell was fully fed. Further validation of the unsteady collective flow model is provided by comparing tracers advected numerically by the feeding cluster of Movie S6 with the actual evolution of the yeast cloud (Movie S15).

5. Dispersion and Mixing Properties of the Collective Feeding Flow

5.1. Cells Dispersion vs. Fluid Dispersion. To further explore the close relationship between locomotion speed v_c and fluid transport efficiency, we quantify the dispersion dynamics of both cells and simulated fluid particles, from the formation of a feeding cluster to its disbanding. As shown in Fig. 2 *A* and *B*, cells initially wandering around soon form a feeding cluster around the yeast injection point. Eight movies lasting $T \approx 3.5$ min each are grabbed approximately every 15 min after food injection at time t_0, up to $t - t_0 = 109$ min. We assume cell behavior is stationary over the duration of each movie. In Fig. 5*A*, the cell MSD for each movie is plotted as a function of $\tilde{t} \in [0, T]$, where $\tilde{t}$ denotes the time elapsed since the start of that specific movie. Regarding the first movie $t - t_0 = 3$ min, the cell MSD (labeled in purple) tends toward a plateau. This behavior is reminiscent of chemotaxis, as cells adapt their locomotion to remain near the injection point after detecting it, contrasting with the Fickian behavior (MSD $\sim 4D_{WF}\tilde{t}$) observed under uniform food conditions, as seen in Section 1. At successive times $t - t_0$ we observe a monotonic growth of the MSDs, which ultimately tend to the faster Fickian regime (MSD $\sim 4D_{NF}\tilde{t}$), as accessible food probably becomes scarcer (SD values for the data shown in Fig. 5*A* are provided in *SI Appendix*, section 11).

To compute fluid dispersion, 2,500 material elements (tracers) are initially arranged on a regular grid at $z_0 = 150\,\mu$m that covers most of the cluster area (*SI Appendix*, section 12A and Movie S16). The tracers are advected using the collective flow computed from the evolving cell positions and orientations collected from every movie. We compute the MSDs in both the xy plane and z-direction. Note that in our system, the average fluid fluctuations decay with distance z from the surface (50). As some tracers are gradually repelled from the surface, the resulting MSDs in both the xy plane and along z will inevitably decrease, to exhibit a subdiffusive regime. Accordingly, we limit the comparison to relative MSDs, bearing in mind that absolute values depend on integration time. In contrast to cell MSDs, tracer MSDs reveal the opposite temporal dynamics: From time $t - t_0 = 15$ min, a diffusive regime is reached with a maximal dispersion coefficient about $D_{Flxy} = 6.10^{-9}$ m^2/s (in comparison, at the same time, $D_{Flz} \approx 8.10^{-10}$ m^2/s = $D_{Flxy}/7.5$; see *SI Appendix*, Fig. S11*B*), before a steady decline of the dispersion coefficient through the successive movies. These opposite spreading dynamics align with previous results, with cell MSDs primarily governed by locomotion speed v_c. The increase in cell MSDs reflects a steady rise in $\langle v_c^2 \rangle$, evident from the evolving velocity distribution (Fig. 5*B*), which gradually shifts from low to high v_c values, i.e. beyond the threshold $v_c^{max} = 500\mu$m/s, above which cells no longer exert a pumping force in the model. As a result, the fraction of feeding cells (i.e. for which $v_c < v_c^{max}$) drops from ~90% just after injection to ~65%, on the way back to the 40% measured prior to injection (see the *Inset* of Fig. 5*B*). As time goes by, fewer cells contribute to the collective flow, and the tracer MSD decreases. The opposing trends between cell MSD and tracer MSD reflect the remarkable behavioral flexibility of *S. lemnae*, which employs a dynamic trade-off between chemotaxis and collective flow to swiftly adapt to ephemeral patches of food.

We compare our simulated fluid dispersion for feeding cells, D_{Flxy}, with an estimate of the fluid dispersion that would result solely from crawling cells. Assuming the cells crawl at the constant speed of $v_c^{free} \approx 770\,\mu$m/s, their far-field flow can be approximated by a stresslet. In this case, we can use the model by Lin et al. (42) whose estimation of the fluid dispersion coefficient κ for a dilute suspension of moving squirmers is dominated by the stresslet flow induced by each squirmer. Using parameters derived from *S. lemnae*'s geometry and considering the equivalent population density as in the movie $t - t_0 = 15$ min (*SI Appendix*, section 12B for further details), we find $\kappa \approx 2.10^{-10}$ m^2/s

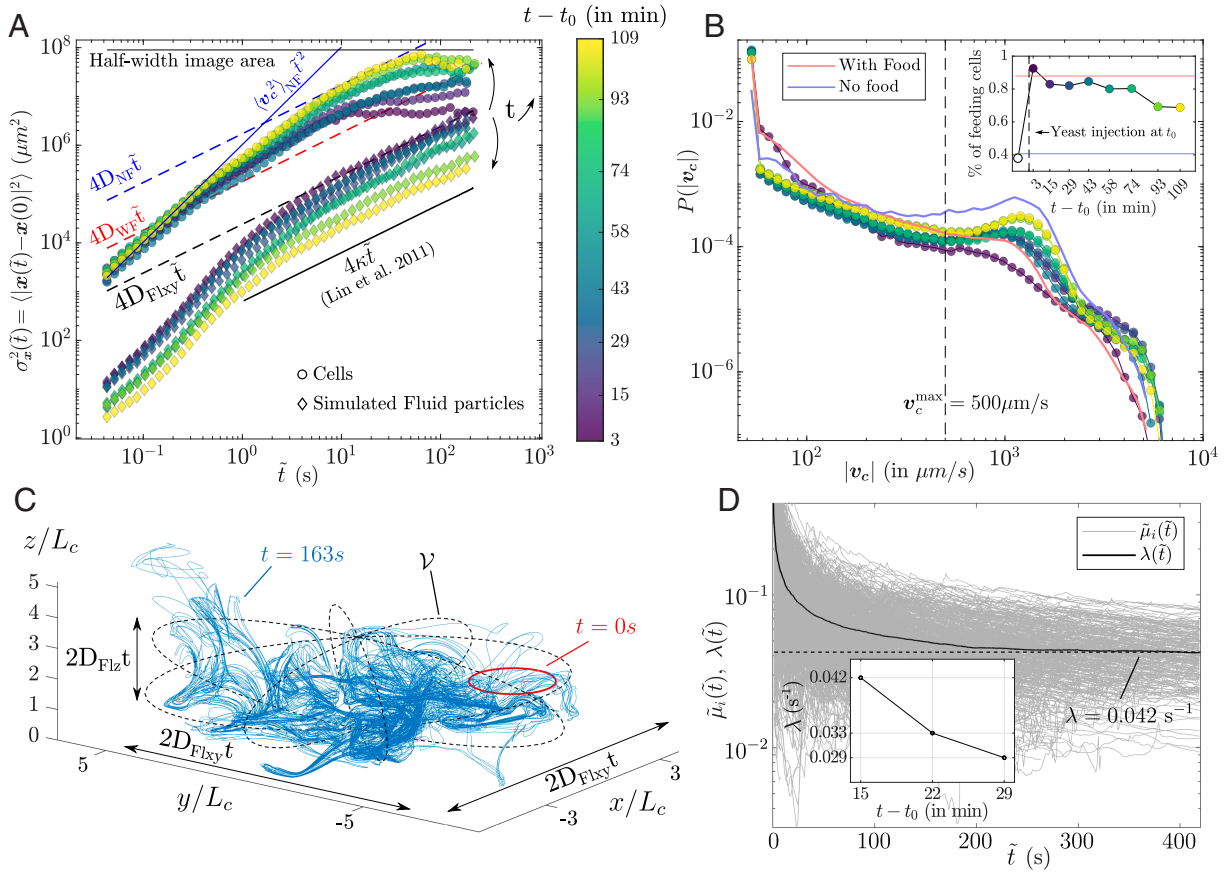

Fig. 5. (*A*) Temporal evolution of the MSDs $\sigma^2_{\tilde{\boldsymbol{x}}}(\tilde{t})$ for both cells and tracers. Each curve is computed over $\tilde{t} \in [0, T]$, at multiples of $(t - t_0) \approx 15$ min, with t_0 the injection time. They are compared to the asymptotic MSDs (dashed lines) extracted from Fig. 1*G* for cells evolving in homogeneous environments (either no-food or with-food conditions), as well as to the model of dispersion by squirmers (42), depicted as a continuous black line. (*B*) $P(|\boldsymbol{v_c}|)$ at successive times $(t - t_0)$ [same colorbar as in (*A*)] and compared to the homogeneous cases from Fig. 1*H*. *Inset*: Proportion of feeding cells over the total number of cells, computed as the fraction of cells with a locomotion velocity $v_c < v_c^{\max}$. (*C*) Material points (tracers) initially arranged on a circle (in red) of length l_0 are advected by the collective flow. After $t = 165$ s the circle is stretched exponentially up to $\rho = l/l_0 \approx 650$ into the blue material line [computed using the Diffusive Strip Method (49)]. (*D*) Temporal evolution of $\tilde{\mu}_i(\tilde{t})$, and their average $\lambda(\tilde{t})$, converging to the value $\lambda \approx 0.042\,\mathrm{s}^{-1}$, for the movie at $t - t_0 = 15$ min. *Inset*: λ values for the three successive movies at early times $t - t_0 = [15, 22, 29]$ min.

that is about 30 times smaller than $D_{Flxy} = 6.10^{-9}$ m^2/s. This stark contrast confirms the much higher fluid transport efficiency of *S. lemnae*'s collective feeding flows compared to their crawling-induced flow. Additionally, note that κ is probably overestimated, as the model by Lin et al. (42) ignores effects of the no-slip wall that increase velocity fluid decay from $v \sim 1/r^2$ to $v \sim 1/r^3$.

Finally, we find that food spreading is even faster when the feeding cluster is already established. We performed the simple experiment of a second yeast injection near an existing feeding cluster formed by a prior injection (*SI Appendix*, section 13A and Movie S17). From the second injection time, we computed both cell and tracer MSDs as in Section 5 (*SI Appendix*, section 13B). While cell MSDs display a subdiffusive behavior indicative of some chemotactic response, tracer MSDs exhibit a persistent superdiffusive regime over 2.5 decades in time as $\sigma^2_{\boldsymbol{x}} = \langle|\boldsymbol{x}(t) - \langle\boldsymbol{x}(t)\rangle|^2\rangle \sim t^{1.6}$. This anomalous scaling reflects persistent hydrodynamic interactions, which enhance food transport efficiency via preferential flow paths.

5.2. Fluid Stretching. Fluid dispersion is linked here to chaotic mixing. Indeed, while feeding, *S. lemnae* continues to perform stochastic reorientations. In this way, the 2D manifolds acting as barriers to transport are regularly destroyed while new ones are built. The ensuing unsteady flow imparts stretching and folding of the fluid elements, the hallmark of chaotic advection most favorable to fluid mixing (51), which we quantify here. For example, Fig. 5*C* illustrates how an initial material line is stretched exponentially by the collective flow into a complex lamellar structure (Movie S18). To quantify the deformation rate, we typically compute the infinite-time Lyapunov exponent, defined as the median stretching rate $\lambda = \lim_{t\to\infty} \ln \rho(t)/t$ with $\rho(t) = l(t)/l(0)$ and $l(t)$ the length of the material line. However, in open flows $\lambda = 0$. Indeed, at some time all fluid particles will be expelled along z out of the influence zone of the pumping flow, where velocity fluctuations vanish. In other words, the unstable manifold is not space-filling anymore but has a fractal dimension, prior to escaping the influence zone (52, 53), that we call mixing region. Consequently, we rather compute the average of the finite-time Lyapunov exponents (FTLEs), evaluated along trajectories as long as they remain inside the mixing region. We define the mixing region as the volume delimited by the minimal envelope surrounding the evolving feeding cluster in the xy plane, and by a height limit $z_{\lim}$ (*SI Appendix*, section 14). Choosing $z_{\lim}$ is delicate as it sets the limit of integration of the FTLEs which decay with z. We set $z_{\lim} = 20h$ based on the measurement that only 8% of the fluid particles are lost beyond $z_{\lim}$ after the $T = 3.5$ min duration of the movie taken at $t - t_0 = 15$ min, implying that the defined mixing region captures nearly all

Lagrangian kinematics over that period (*SI Appendix*, Fig. S13*B* and Fig. 5*C*). Regarding the movie $t-t_0 = 15$ min, we compute FTLEs $\tilde{\mu}_i(\tilde{t})$ along trajectories i within the mixing region, and take their average $\lambda(\tilde{t}) = \langle\tilde{\mu}_i(\tilde{t})\rangle$. Fig. 5*D* shows convergence to $\lambda \approx 0.042\,\mathrm{s}^{-1}$ after $\tilde{t} = 2T$ (see *SI Appendix*, section 15 for further details about FTLEs computation, and Movie S19). This convergence was also achieved for three successive movies at early times $t-t_0 = [15, 22, 29]$ min (note that we incorporate here the movie $t-t_0 = 22$ min, not considered in the previous section), as can be observed on the *Inset* of Fig. 5*D* which shows a decay of λ in time, in parallel to the regular decay of the MSDs for the fluid particles. Here too, the decay of λ over time results from fewer cells contributing to the collective flow. Last, the Lyapunov exponent λ is made dimensionless as $\lambda\tau_c$, where τ_c is the average feeding period between fast crawling events (i.e. for which $v_c < v_c^{\max}$). Regarding the movie $t-t_0 = 15$ min, we find $\tau_c \approx 2.1$ s, yielding a dimensionless Lyapunov exponent $\lambda\tau_c \approx 0.09$. The dimensionless λ enables comparison of the chaotic strength of the collective flow to known passive laminar chaotic flows and to notice that *S. lemnae* performs well (for the given mixing region): less than random porous media [$\lambda \approx 0.21$ (54)], or sheared particulate suspension [$\lambda \approx 0.21$ for a solid volume fraction of $\phi = 0.35$ (55)], but better than ordered porous media [$\lambda \approx 0.073$ (56)].

5.3. Mixing Time and Coalescence Time. We provide here characteristic times indicative of the fluid mixing rate by the collective flow, using the lamellar approach (35, 49). This theoretical framework describes evolving concentration fields as a set of stretched filaments (lamellae), where the concentration within each lamella is governed by the coupling between its stretching history ρ and molecular diffusion D. In 3D flows, mixtures form 3D sheets whose material area elements align with the principal strain directions, while the compression direction lies mainly perpendicular to the surface (57, 58). Fluid incompressibility dictates that the sheet width decays as ρ^{-1}, until enhanced diffusion and compression balance the sheet width down to the Batchelor scale s_b, corresponding to the mixing time t_s. In chaotic flows, 3D sheets experience a constant elongation rate on average $\dot{\rho}/\rho = \lambda$ so that $\rho \sim e^{\lambda t}$. In such a case, s_b remains constant over time as $s_b = \sqrt{D/\lambda}$, at the mixing time $t_s = (1/2\lambda)\ln(1+2Pe)$. Of course, in our open flow, the parameters s_b, λ and so t_s are in reality space-dependent, varying on average as a function of z. Here, we focus on averages within the mixing region. Taking $\lambda = 0.042\,\mathrm{s}^{-1}$, and $D_{\mathrm{yeast}} = 10^{-11}\,\mathrm{m}^2/\mathrm{s}$, we get $t_s \approx 80$ s. By contrast, purely diffusive mixing of a $s_0 = 500\,\mu$m-thick blob in a still ambient fluid would take $t_s \approx s_0^2/D_{\mathrm{yeast}} = 2.5\times10^4$ s, illustrating how powerful exponential stretching is to accelerate dilution. Later, coalescence of the sheets further accelerate homogenization. Initially well separated, the adjacent sheets inevitably merge as the unfolded blob volume expands faster than the surrounding dispersion volume (35, 59). Since the sheet surface grows exponentially while its thickness is locked at s_b, the unfolded blob volume V in turn increases exponentially as

$$V \sim \frac{4}{3}\pi s_b s_0^2 e^{\lambda t}, \qquad [4]$$

with s_0 the initial blob radius. Meanwhile, the blob is bounded by the dispersion envelope (see scheme of Fig. 5*C*) growing as a power law:

$$\mathcal{V} \sim \frac{4}{3}\pi(s_0^2 + 2D_{Flxy}t)\sqrt{s_0^2 + 2D_{Flz}t} \sim t^{3/2}, \qquad [5]$$

with D_{Flxy} and D_{Flz} computed earlier. The average number of overlaps is given by the ratio $V/\mathcal{V}$. The time at which the lamellae overlap once on average $V/\mathcal{V} = 1$ is referred to as the coalescence time, and for the movie $t-t_0 = 15$ min corresponds to $t_{\mathrm{coal}} \approx 150$ s (*SI Appendix*, Fig. S15). Coalescence further accelerates homogenization toward the mean concentration $\langle C\rangle = C_0/\mathcal{V}$. Importantly, both mixing and coalescence times occur very early compared to the lifespan of the feeding cluster (~1 to 2 h in the present case), underscoring the efficiency of the collective flow in mixing solutes. Also, if some fluid is constantly expelled from the mixing region and exchanged with fresh fluid, at $t_{\mathrm{coal}} = 150$ s only 6% of the fluid particles have left the mixing region (*SI Appendix*, Fig. S12*B*). This suggests that, already at $t-t_0 = 15$ min, most cells within the cluster should probe a similar concentration of food or nutrients. Additionally, a cell arriving at the edge of an already established feeding cluster has in an instant a fair appreciation of the chemical content of the mixing region.

6. Discussion

By organizing into feeding clusters, *S. lemnae* gains the ability to spread and mix fluid over larger scales. One can legitimately ask whether this organization provides benefits to *S. lemnae*, and at what cost: In other words, is the feeding cluster of a cooperative nature? At present, in laboratory conditions, improved foraging success is a potential benefit emerging from our results. It arises from two mechanisms. First, the active spreading of food—driven by and along with the formation of an expanding feeding cluster—increases the probability that still-foraging cells encounter food, scaling with the patch surface as $S \sim \sigma_x^2 \sim D_{Flxy}t$. Second, once a feeding cluster is established, it gains the ability to spread any neighborhood food source even faster throughout the cluster, with superdiffusive scaling $S \sim \sigma_x^2 \sim t^{1.6}$. Both mechanisms hasten the spatial overlap between the distributions of cells and food, increasing the probability of interactions between them. Whether this increased probability of interaction actually leads to an enhanced feeding efficiency per cell within the group remains a compelling hypothesis to be tested by future studies. Furthermore, it is not yet known to what extent these enhanced interactions apply under natural conditions, for example if cells crawl on more complex solid surfaces or are exposed to external flows.

As for the costs of maintaining collective flows, our preliminary estimate is that they are not significant. As mentioned above, collective flows arise primarily from the reduction in locomotion speed v_c of cells clustered around a food patch. Modulating locomotion velocity is a well-known chemotactic strategy that is sufficient to explain the individual behavior of cells. Furthermore, near a food patch, *S. lemnae* behaves similarly whether isolated or as part of a cluster. In all cases, it remains in the food patch, its feeding flow does not weaken and persists beyond cell satiety. The most notable distinction arises from the physical contacts that inevitably occur as cells cluster together. These contacts elicit avoidance reactions, which manifest as SSR moves that may propagate across the population. Far from having a negative impact, this effect could help maintain minimal spacing between cells, allowing for more efficient spatial coverage by the cluster. Whether this phenomenon represents a form of self-organization will be the subject of future research. Regarding the collective flow itself, while it is true that its dilution effect could be counterproductive in terms of feeding efficiency if the initial concentration were low, this is not a concern here given the initially high concentration.

Thus, since potential benefits appear to outweigh costs, we believe that the feeding cluster represents a form of cooperative behavior employed by *S. lemnae*. Until further investigation uncovers more active forms of cooperation such as active signaling or enhanced feeding rates per cell, we recognize here a type of intraspecific cooperation termed by-product cooperation. Such cooperation could apply to other Spirotrich species, as we have observed similar behavioral patterns in *S. mytilus* and *Euplotes vannus*. More broadly, the hydrodynamic cooperation observed in *S. lemnae* shares striking similarities with that of previously cited organisms, namely *T. majus* and *Uronemella* (29–31): In all cases, clusters form in response to resource gradients, leading to long-range flows. Similarly, just as collective flows in *T. majus* and *Uronemella* depend on variations in population density driven by individual random walks, chaotic mixing in our system would not occur without stochastic reorientations of the cells. The main difference lies in the lack of physical bonds between individuals in the *S. lemnae* cluster, which likely enables them to adapt faster to dynamic environments and efficiently exploit localized ephemeral patches. In contrast, colonies such as *volvox* or choanoflagellates, which take hours to form, would be better suited for larger and persistent patches.

To help reconcile predictions of feeding rates with experimental observations for different cell organizations in a patchy food environment, as discussed in the Introduction, our results suggest that the unsteady nature of the feeder's motion may play an important role. Not only does this dynamic stochastic motion affect chemotaxis, but it also allows chaotic flows to occur, shaping resource distribution considerably. In fact, the oscillations observed between members of a *Stentor* cluster (60), the erratic contractions of *Vorticella* (10), the alternating cilia beat regime of *Oocystis asymmetrica* (18), or the stochastic and uncorrelated beating of flagella in *Salpingoeca rosetta* colonies (61), may just be additional examples of stochastic motions primarily evolved to induce chaotic flow. Future studies would benefit from incorporating cell stochastic motion into their models, as ignoring it imposes overly restrictive topological constraints on the Lagrangian kinematics and precludes chaos.

7. Conclusions and Perspectives

We described the cooperative foraging behavior of *S. lemnae* in a patchy environment. Upon discovering a food patch, *S. lemnae* reduces its locomotion speed v_c, thus increasing the range of its feeding flow. As cells cluster around the patch, individual feeding flows interact hydrodynamically, leading to a collective unsteady flow at the population scale. By combining experimental and numerical methods, we measured and predicted the full 3D unsteady flow, and quantified its transport and mixing properties. Our results show that the feeding cluster is at least 30 times more efficient at spreading fluid than a suspension of swimmers and that the Lyapunov exponent of the cluster's flow is comparable to that of known nonbiological chaotic flows. Given the potential benefits granted by collective fluid spreading and mixing without additional apparent costs, we propose that the feeding group exemplifies by-product cooperation. This study establishes a quantitative framework for understanding the highly dynamical interplay between an organism's behavior and the spatial distribution of a resource that it actively shapes. In particular, we hypothesize that optimal feeding in cell clusters in patchy environments relies more on the fluid stirring protocol than on the mere sum of individual scanning fluxes. Many aspects of a feeding cluster remain to be explored: For instance, does the cluster organization enhance the average feeding rate per cell? Could it reflect underlying coordinated cooperative behavior, such as quorum sensing driven by active chemical signaling? How might the cluster adapt to varying food properties (e.g. food dispersion coefficients), different surface architectures (like porous media), or ambient conditions (such as background flow, or confinement)? How does the cluster respond to predator repellents?

8. Materials and Methods

8.1. Cell Culture. Strains of *S. lemnae* were provided by Dieter Ammermann (Tübingen, Germany). Cultures were maintained within 10 ml of Eau Volvic at 15 °C under a 12:12 h light:dark cycle. They were fed twice a week with the alga *Chlorogonium sp.* and occasionally with yeast. Fresh cultures were established every two weeks by transferring about 30 cells into new culture medium.

8.2. Experimental Setting. Before experimentation, cells were transferred to a Petri dish and acclimated to 20 °C. Prior to each experiment, cells were starved for 24 h. Six experiments were conducted (see *SI Appendix* for details). The experiments on locomotion behavior (*SI Appendix*, section 1 and first half of *SI Appendix*, section 2) and cells dispersion (*SI Appendix*, section 5) were performed directly in their Petri dish culture, using the large field of view provided by a stereo microscope (Olympus SZX16), equipped with a Photron Fastcam Mini UX100 camera and a 0.7× or 0.8× optical objective. Experiments requiring finer spatial resolution–namely, the measurements of single flows (*SI Appendix*, section 3) and collective flow (*SI Appendix*, section 4)–were performed in an observation chamber consisting of two parallel glass plates separated by a 3 mm gap, placed on an inverted Olympus IX81 microscope. For the collective flow experiment, images were captured using a low readout-noise camera (Hamamatsu ORCA Fusion BT camera). Finally, the dye tracer experiment (*SI Appendix*, section 2) was conducted with cells in the observation chamber, and imaging performed using the Hamamatsu ORCA fusion BT camera mounted on the stereo Olympus SZX16 microscope, with a 0.8× objective.

8.3. Image Processing. Image processing was performed using in-house developed MATLAB (MathWorks) programs. Cell trajectories were reconstructed using the MATLAB PTV code by Blair and Dufresne (62). PIV analysis was performed using the PIVlab MATLAB program.

Data, Materials, and Software Availability. The data supporting the findings of the study are included in the article and in the supporting information. The raw data related to the study and the relevant MATLAB codes are available at: https://hdl.handle.net/20.500.12928/EP90AW (63).

ACKNOWLEDGMENTS. We are deeply grateful to Dieter Ammermann for providing us with *S. lemnae*. We thank Elena Di Poi for backup cultures. R.T. thanks Nicolas Salles, Nina Javerzat, Benjamin Walter, Bloen Metzger, and Henri Lhuissier for helpful discussions. We gratefully acknowledge the support by the European Research Council through the European Research Council Proof of Concept Grant Stripe-o-Morph (GA 101069436) and by the Italian Ministry of Research through the projects Response (PRIN 2020), Abyss (PRIN 2022), and Green-Swarm-Intelligence (PRO3).

Author affiliations: [a]The Biorobotics Institute, Scuola Superiore Sant'Anna, Pisa 56025, Italy; [b]Mathlab, International School for Advanced Studies, Trieste 34136, Italy; and [c]Sezione Oceanografia, Istituto Nazionale di Oceanografia e di Geofisica Sperimentale, Trieste 34151, Italy

1. T. Kiørboe, *A Mechanistic Approach to Plankton Ecology* (Princeton University Press, 2008).
2. R. Stocker, Marine microbes see a sea of gradients. *Science* **338**, 628–633 (2012).
3. J. R. Seymour, M. R. Stocker, Resource patch formation and exploitation throughout the marine microbial food web. *Am. Nat.* **173**, 02139 (2009).
4. Y. Yawata, F. Carrara, F. Menolascina, R. Stocker, Constrained optimal foraging by marine bacterioplankton on particulate organic matter. *Proc. Natl. Acad. Sci. U.S.A.* **117**, 25571–25579 (2020).
5. R. E. Breier, C. C. Lalescu, D. Waas, M. Wilczek, M. G. Mazza, Emergence of phytoplankton patchiness at small scales in mild turbulence. *Proc. Natl. Acad. Sci. U.S.A.* **115**, 12112–12117 (2018).
6. J. S. Guasto, K. A. Johnson, J. P. Gollub, Oscillatory flows induced by microorganisms swimming in two dimensions. *Phys. Rev. Lett.* **105**, 189901 (2010).
7. D. Tam, A. E. Hosoi, Optimal feeding and swimming gaits of biflagellated organisms. *Proc. Natl. Acad. Sci. U.S.A.* **108**, 1001–1006 (2011).
8. S. Michelin, E. Lauga, Optimal feeding is optimal swimming for all péclet numbers. *Phys. Fluids* **23**, 1–14 (2011).
9. R. E. Pepper *et al*., A new angle on microscopic suspension feeders near boundaries. *Biophys. J.* **105**, 1796–1804 (2013).
10. S. Ryu, R. E. Pepper, M. Nagai, D. C. France, Vorticella: A protozoan for bio-inspired engineering. *Micromachines* **8**, 1–25 (2017).
11. K. Y. Wan *et al*., Reorganization of complex ciliary flows around regenerating stentor coeruleus. *Philos. Trans. R. Soc. B Biol. Sci.* **375**, 20190167 (2020).
12. E. A. Kanso, R. M. Lopes, J. Rudi Strickler, J. O. Dabiri, J. H. Costello, Teamwork in the viscous oceanic microscale. *Proc. Natl. Acad. Sci. U.S.A.* **118**, 1–6 (2021).
13. M. Rode, T. Kiørboe, A. Andersen, Feeding flow and membranelle filtration in ciliates. *Phys. Rev. Fluids* **7**, 023102 (2022).
14. T. Kiørboe, What makes pelagic copepods so successful? *J. Plankton Res.* **33**, 677–685 (2011).
15. C. A. Solari, S. Ganguly, J. O. Kessler, R. E. Michod, R. E. Goldstein, Multicellularity and the functional interdependence of motility and molecular transport. *Proc. Natl. Acad. Sci. U.S.A.* **103**, 1353–1358 (2006).
16. M. Roper, M. J. Dayel, R. E. Pepper, M. A. Koehl, Cooperatively generated stresslet flows supply fresh fluid to multicellular choanoflagellate colonies. *Phys. Rev. Lett.* **110**, 1–5 (2013).
17. J. B. Kirkegaard, R. E. Goldstein, Filter-feeding, near-field flows, and the morphologies of colonial choanoflagellates. *Phys. Rev. E* **94**, 052401 (2016).
18. C. Hartmann, Ö. Özmutlu, H. Petermeier, J. Fried, A. Delgado, Analysis of the flow field induced by the sessile peritrichous ciliate *Opercularia asymmetrica*. *J. Biomech.* **40**, 137–148 (2007).
19. A. J. Mathijssen, J. Culver, M. S. Bhamla, M. Prakash, Collective intercellular communication through ultra-fast hydrodynamic trigger waves. *Nature* **571**, 560–564 (2019).
20. C. Dombrowski, L. Cisneros, S. Chatkaew, R. E. Goldstein, J. O. Kessler, Self-concentration and large-scale coherence in bacterial dynamics. *Phys. Rev. Lett.* **93**, 2–5 (2004).
21. I. Tuval *et al*., Bacterial swimming and oxygen transport near contact lines. *Proc. Natl. Acad. Sci. U.S.A.* **102**, 2277–2282 (2005).
22. M. B. Short *et al*., Flows driven by flagella of multicellular organisms enhance long-range molecular transport. *Proc. Natl. Acad. Sci. U.S.A.* **103**, 8315–8319 (2006).
23. A. Andersen, T. Kiørboe, The effect of tethering on the clearance rate of suspension-feeding plankton. *Proc. Natl. Acad. Sci. U.S.A.* **117**, 30101–30103 (2020).
24. K. K. Christensen-Dalsgaard, T. Fenchel, Increased filtration efficiency of attached compared to free-swimming flagellates. *Aquat. Microb. Ecol.* **33**, 77–86 (2003).
25. R. A. Alegado *et al*., A bacterial sulfonolipid triggers multicellular development in the closest living relatives of animals. *eLife* **2012**, e00013 (2012).
26. T. Fenchel, Microbial behavior in a heterogeneous world. *Science* **296**, 1068–1071 (2002).
27. J. R. Blake, S. R. Otto, D. A. Blake, Filter feeding, chaotic filtration, and a blinking stokeslet. *Theor. Comput. Fluid Dyn.* **10**, 23–36 (1997).
28. B. A. Orme, S. R. Otto, J. R. Blake, Enhanced efficiency of feeding and mixing due to chaotic flow patterns around choanoflagellates. *IMA J. Math. Appl. Med. Biol.* **18**, 293–325 (2001).
29. T. Fenchel, R. N. Glud, Veil architecture in a sulphide-oxidizing bacterium enhances countercurrent flux. *Nature* **394**, 367–369 (1998).
30. A. Petroff, A. Libchaber, Hydrodynamics and collective behavior of the tethered bacterium *Thiovulum majus*. *Proc. Natl. Acad. Sci. U.S.A.* **111**, E537–E545 (2014).
31. A. P. Petroff, A. L. Pasulka, N. Soplop, X. L. Wu, A. Libchaber, Biophysical basis for convergent evolution of two veil-forming microbes. *R. Soc. Open Sci.* **2**, 2150437 (2015).
32. D. Ammermann, M. Schlegel, Characterization of two sibling species of the genus *Stylonychia* (Ciliata, Hypotricha): *S. mytilus* Ehrenberg, 1838 and *S. lemnae* n. sp. I. Morphology and reproductive behavior. *J. Protozool.* **30**, 290–294 (1983).
33. P. Madoni, Protozoa in wastewater treatment processes: A minireview. *Italian J. Zool.* **78**, 3–11 (2011).
34. W. E. Ranz, Applications of a stretch model to mixing, diffusion, and reaction in laminar and turbulent flows. *AIChE J.* **25**, 41–47 (1979).
35. E. Villermaux, Mixing versus stirring. *Annu. Rev. Fluid Mech.* **51**, 245–273 (2019).
36. N. Ricci, R. Giannetti, C. Miceli, The ethogram of *Euplotes crassus* (ciliata, hypotrichida): I. The wild type. *Eur. J. Protistol.* **23**, 129–140 (1988).
37. N. Ricci, Locomotion as a criterion to read the adaptive biology of protozoa and their evolution toward metazoa. *Boll. Zool.* **56**, 245–263 (1989).
38. J. R. Lawrence, R. A. Snyder, Feeding behaviour and grazing impacts of a Euplotes sp. On attached bacteria. *Can. J. Microbiol.* **44**, 623–629 (1998), 10.1139/w98-057.
39. H. C. Berg, *E. coli in Motion* (Springer, 2004).
40. N. Liron, S. Mochon, Stokes flow for a stokeslet between two parallel flat plates. *J. Eng. Math.* **10**, 287–303 (1976).
41. J. Ainley, S. Durkin, R. Embid, P. Boindala, R. Cortez, The method of images for regularized stokeslets. *J. Comput. Phys.* **227**, 4600–4616 (2008).
42. Z. Lin, J. L. Thiffeault, S. Childress, Stirring by squirmers. *J. Fluid Mech.* **669**, 167–177 (2011).
43. R. Cortez, D. Varela, A general system of images for regularized stokeslets and other elements near a plane wall. *J. Comput. Phys.* **285**, 41–54 (2015).
44. J. S. Guasto, R. Rusconi, R. Stocker, Fluid mechanics of planktonic microorganisms. *Annu. Rev. Fluid Mech.* **44**, 373–400 (2011).
45. K. Drescher, J. Dunkel, L. H. Cisneros, S. Ganguly, R. E. Goldstein, Fluid dynamics and noise in bacterial cell-cell and cell-surface scattering. *Proc. Natl. Acad. Sci. U.S.A.* **108**, 10940–10945 (2011).
46. G. Haller, Lagrangian coherent structures. *Annu. Rev. Fluid Mech.* **47**, 137–162 (2015).
47. A. Surana, O. Grunberg, G. Haller, Exact theory of three-dimensional flow separation. Part 1. Steady separation. *J. Fluid Mech.* **564**, 57–103 (2006).
48. R. S. MacKay, Transport in 3D volume-preserving flows. *J. Nonlinear Sci.* **4**, 329–354 (1994).
49. P. Meunier, E. Villermaux, The diffusive strip method for scalar mixing in two dimensions. *J. Fluid Mech.* **662**, 134–172 (2010).
50. F. Guzmán-Lastra, H. Löwen, A. J. Mathijssen, Active carpets drive non-equilibrium diffusion and enhanced molecular fluxes. *Nat. Commun.* **12**, 1906 (2021).
51. J. M. Ottino, *The Kinematics of Mixing: Stretching, Chaos, and Transport* (Cambridge University Press, 1989).
52. T. Tél, A. de Moura, C. Grebogi, G. Károlyi, Chemical and biological activity in open flows: A dynamical system approach. *Phys. Rep.* **413**, 91–196 (2005).
53. E. Gouillart, O. Dauchot, J. L. Thiffeault, Measures of mixing quality in open flows with chaotic advection. *Phys. Fluids* **23**, 1–12 (2011).
54. J. Heyman, D. R. Lester, R. Turuban, Y. Meheust, T. L. Borgne, Stretching and folding sustain microscale chemical gradients in porous media. *Proc. Natl. Acad. Sci. U.S.A.* **117**, 13359–13365 (2020).
55. M. Souzy, H. Lhuissier, E. Villermaux, B. Metzger, Stretching and mixing in sheared particulate suspensions. *J. Fluid Mech.* **812**, 611–635 (2017).
56. R. Turuban, D. R. Lester, T. L. Borgne, Y. Méheust, Space-group symmetries generate chaotic fluid advection in crystalline granular media. *Phys. Rev. Lett.* **120**, 024501 (2018).
57. D. Martínez-Ruiz, P. Meunier, B. Favier, L. Duchemin, E. Villermaux, The diffusive sheet method for scalar mixing. *J. Fluid Mech.* **837**, 230–257 (2018).
58. P. Meunier, E. Villermaux, The diffuselet concept for scalar mixing. *J. Fluid Mech.* **951**, A33 (2022).
59. R. Turuban, H. Lhuissier, B. Metzger, Mixing in a sheared particulate suspension. *J. Fluid Mech.* **916**, R4 (2021).
60. S. Shekhar *et al*., Cooperative hydrodynamics accompany multicellular-like colonial organization in the unicellular ciliate stentor. bioRxiv [Preprint] (2023). https://doi.org/10.1101/2023.01.10.523506 (Accessed 21 November 2024).
61. J. B. Kirkegaard, A. O. Marron, R. E. Goldstein, Motility of colonial choanoflagellates and the statistics of aggregate random walkers. *Phys. Rev. Lett.* **116**, 038102 (2016).
62. D. Blair, E. Dufresne, The matlab particle tracking code repository (2005). https://site.physics.georgetown.edu/matlab/.
63. R. Turuban, G. Noselli, A. Beran, A. DeSimone, Cooperative mixing in Stylonychia lemnae. SISSA Open Data. https://hdl.handle.net/20.500.12928/EP90AW. Deposited 22 August 2025.